ORIGINAL ARTICLE

Tailoring the mechanical properties of binary polypropylene blends with polymorphic and oriented hierarchical structures

Yan Wang[1,2] · Yisu Wang[1] · Shuai Qiu[1] · Hong Zhang[1] · Jing Guo[1] · Jia-Zhuang Xu[2]

Abstract

Ziegler-Natta isotactic polypropylenes (ZN-iPP) were melt blended with metallocene-based isotactic polypropylenes (M-iPP) to regulate and strengthen their mechanical properties systematically. Quantitatively, the hierarchical structure was characterized by synchrotron wide-angle X-ray diffraction, small-angle X-ray scattering, and differential scanning calorimetry. Without specific catalysts, the iPP samples exhibited a continuous change in the tensile strength (26.9–49.5 MPa) and impact strength (4.7–23.2 KJ/m^2). With variable composition, the iPP blends exhibited mechanical properties that were related to the complex lamellar morphology, which is characterized by a gradually changing ratio of γ- to α-crystals and a continuous change in lamellar thickness. Compared to conventional injection molding samples, the oscillatory shear injection molding samples were simultaneously reinforced and toughened at a given blend composition, which was attributed to the shish-kebab structure (containing the α-parent crystal, α-daughter crystal, γ-crystals) and the relatively thicker lamellar thickness throughout the samples. The regulatory capacity of strength, ductility, and toughness of the iPP blends in this work is outstanding, providing an avenue to use iPP more efficiently, which should be valuable in industrial applications.

Introduction

Polypropylene is a universal polymer that is being increasingly produced, and the global output of polypropylene in 2021 was 100 million tons. Adding polyolefin to achieve balanced mechanical performance and/or to recycle polypropylene [1, 2] is a common and effective way to expand its application, and one strategy is to mix aPP/iPP [3], PE/iPP [4, 5] and iPP1/iPP2 [6, 7]. Characterized by polymorphic and hierarchical structures, binary iPP blends are more complex. Thus, the solidification processing of iPP and its accompanying hierarchical structure and mechanical properties have received continuous attention from the academic and industrial sectors [8, 9].

The relationship between the polymorphs (α-, β- and γ-phases) and the mechanical properties of iPP has been well established, e.g., α-iPP can provide strong mechanical properties [10, 11], β-iPP could greatly improve its toughness [12], while γ-crystals demonstrate a higher modulus and higher yield stress [13]. The mechanical behavior of the abovementioned crystal structure is strongly influenced by the chain microstructure. Generally, Ziegler-Natta iPP (ZN-iPP) is synthesized by the traditional heterogeneous Ziegler-Natta catalyst, which always presents α-crystals. Compared to the widely used ZN-iPP counterparts, metallocene-based isotactic iPP (M-iPP) is a relatively nascent isotactic polypropylene that tends to crystallize into γ-crystals [14]. The blends of commercial M-iPP and ZN-iPP families are frequently encountered; thus, the blends used in this paper are a typical example of these two categories of mixtures. In this investigation, roughly the same molecular mass of M-iPP and ZN-iPP is selected, while the molecular weight distribution with polydispersity index is

✉ Yan Wang
  wwangyan@dlpu.edu.cn

✉ Jia-Zhuang Xu
  jzxu@scu.edu.cn

1   School of Textile and Material Engineering, Dalian Polytechnic University, Dalian 116034, China

2   College of Polymer Science and Engineering and State Key Laboratory of Polymer Materials Engineering, Sichuan University, Chengdu 610065, China

approximately 2 for M-iPP and between 4 and 7 for ZN-iPP. The structure and properties of the M-iPP and ZN-iPP blends were investigated systematically on the basis of the composition ratios. The possibility of obtaining materials with a series of properties varying from those of ZN-iPP to those of M-iPP could be pursued by merely changing the composition of the blend.

Of course, controlling the material properties by mixing the two types of iPP strictly depends on polymer processing [15]. Conventional polymer processing generally involves the applications of stress fields and varying temperatures, which consequently affect the motion of polymer chains and their ability to form primary nuclei and the resultant morphology. Taken together, both molecular architecture and processing have a significant impact on the polymorphism and morphology, which governs the macroscopic mechanical properties of polypropylene blends.

In this research, the polymorphic behavior of M-iPP/ZN-iPP blends was investigated by conventional injection molding (CIM) and oscillatory shear injection molding (OSIM). Synchrotron wide-angle X-ray diffraction (WAXD), small-angle X-ray scattering (SAXS), and differential scanning calorimetry (DSC) were used to characterize the crystalline and hierarchical structure of blends and to inspect the influences of the varied composition and processing. The mechanical properties of the injection-molded samples were measured by the combination of tensile and notched Izod impact tests. The change in mechanical performance depends on the blend ratio, with the performance varying from the high stiffness of the neat ZN-iPP to the ductility of the neat M-iPP. The mechanical performance stems from the complex lamellar morphology, characterized by the gradually changing ratio of γ- to α-crystals and the continuous change in lamellar thickness. Furthermore, compared to CIM, the OSIM samples at a given blend composition exhibited greater reinforcement and toughening, which is attributed to the shish-kebab structure (containing the α-parent crystal, α-daughter crystal, γ-crystals) in the whole sample. The regulatory capacity of the strength, ductility, and toughness of the iPP blends is outstanding in this work, providing an avenue to more efficiently use iPP, which should be valuable in industrial applications.

Experimental section

Material

ZN-iPP polymerized by the Ziegler-Natta catalyst (T30S) was purchased from Dushanzi Petroleum Chemical Co., China, while the M-iPP synthesized by the metallocene catalyst was supplied by Basel Co., The Netherlands. The main parameters are presented in Table 1.

**Table 1** Characteristic parameters of the molecular chain for ZN-iPP and M-iPP

	M_w (g/mol)	M_w/M_n	Melt flow rate (MFR) (230 °C, 21.6 N)	[mm] %
ZN-iPP	39.9×10^4	4.6	3 g/10 min	97.5
M-iPP	40.7×10^4	2.25	12 g/10 min	96.05

Sample preparation

First, M-iPP and ZN-iPP were melt mixed by a twin-screw extruder to form blending pellets. The screw speed was set to 80 rpm, and the screw temperature was set to 170–180 °C from hopper to nozzle. After drying, the extruded pellets were injected into a mold with OSIM technology [16], forming the standard tensile specimen with a double-bone shape and a neck size of 30 mm × 6 mm × 4 mm and impact test samples with a size of 50 mm × 10 mm × 4 mm. For OSIM technology, continuous oscillatory shear was exerted at the packing stage in an injection-molded cycle. A detailed description of OSIM technology has previously been reported [16]. Specifically, the iPP melt experienced persistent repetition of shear stress using two pistons until the melt solidified. During the holding period, if the movements of the two pistons were not synchronized, an oscillatory shear force was generated, causing the iPP melt to be shaped reciprocally along the length of the mold. This process subjected the iPP melt to repeated shear stress until the pistons stopped just before solidification. Herein, the oscillation shear frequency of 0.3 Hz with a pressure of 120 bar and a molding temperature of 40 °C was applied, and the injection temperature profile of 170–210 °C was set. The counterparts of CIM were acquired under the same processing conditions only without oscillatory shear. Blends with compositions of 0/100, 10/90, 30/70, 50/50, 70/30, 90/10, and 100/0 wt %/wt % of M-iPP and ZN-iPP were prepared. The M-iPP/ZN-iPP blend was designated MZxy, in which x and y are the weight ratios of M-iPP and ZN-iPP, respectively.

X-ray diffraction (scattering) characterization

BL15U and BL 16B of the Shanghai Synchrotron Radiation Facility, China, were used to perform WAXD and SAXS measurements. The wavelength of the X-ray (λ) was 1.24 Å. The X-ray beam could be concentrated in an area of $3 \times 2.7 \, \mu m^2$ (length × width) for WAXD and $28 \times 20 \, \mu m^2$ for SAXS. WAXD images were collected by a MAR 345 image plate detector (MAR Research Co. Ltd., Germany). The sample was prepared from the central part of a dumbbell bar, as shown in Fig. 1. The 4-mm thick sample was machined into a thin lamina (thickness of 1 mm and width of 6 mm) using common method sandpaper grinding.
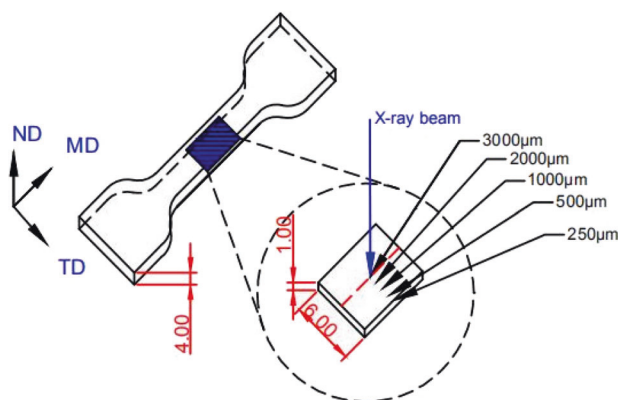
Fig. 1 Spatial location diagram of the specimens for the 2D WAXD and SAXS measurements (MD, the flow direction; TD, the transverse direction; ND, the normal direction of the MD-TD plane)

Six locations [250 and 500 μm (skin layer), 1000 and 2000 μm (intermediate layer), and 3000 μm (core layer)] were measured down from the surface of MD-TD by WAXD and SAXS.

The molecular orientation was quantified by Hermans' orientation function, which is defined as follows:

$$f_H = \frac{3\langle\cos^2\varphi\rangle - 1}{2} \tag{1}$$

where the orientation factor $(\cos^2\varphi)$ is calculated by

$$\langle\cos^2\varphi\rangle = \frac{\int_0^{\pi/2} I(\varphi)\cos^2\varphi\sin\varphi d\phi}{\int_0^{\pi/2} I(\varphi)\sin\varphi d\varphi} \tag{2}$$

where $I(\varphi)$ is the intensity and φ is the angle between the flow direction and the normal of a given crystal plane (hkl). The orientation parameter was calculated by Picken's method at $q = 9.70\,\text{Å}^{-1}$ (i.e., 040 and 008 reflections) of WAXD [17].

Differential scanning calorimetry (DSC)

The thermal behavior of M-iPP/ZN-iPP blends was tested with a calorimeter (TA DSC Q200). Samples weighing 5~8 mg were obtained from different layers of bars roughly corresponding to the WAXD location and scanned in the range of 40–200 °C at a rate of 10 °C/min under an N₂ atmosphere. On the other hand, crystallization thermograms were first melted at 200 °C for 3 min to remove the thermal history and then cooled to 80 °C at a rate of 10 °C/min in an N₂ atmosphere.

Mechanical property testing

The tensile performance of the specimens was measured at 23 ± 2 °C using an Instron Instrument Model 5576 (ASTM D-638, cross-head speed of 50 mm/min). The tensile modulus

was determined at a strain of 1% in the Hookean elastic region. Izod impact tests were measured following ASTM D256-05 using specimens with dimensions of 50 mm × 10 mm × 4 mm and a V-notch of 2.0 mm depth. Five or six replicates were tested for each sample, and the average value was presented with the standard deviation.

Results

Hierarchical crystalline morphology and its distribution

2D WAXD with a microfocus function was performed to evaluate the spatially distributed crystalline structure of injection-molded blended samples. Figure 2 shows the spatial distribution of the 2D WAXD patterns (i.e., from the surface to the core along the TD direction, as shown in Fig. 1) of the OSIM and CIM samples. All OSIM sample patterns showed a distinct azimuthal dependence, indicating a crystalline orientation throughout the OSIM samples. In comparison, the CIM samples only showed strong azimuthal dependence at 250 and 500 μm, while the diffraction at other positions exhibited an unobvious azimuth orientation. For all of the patterns, six rings of diffraction corresponding to different lattice planes of iPP were observed. The specific diffractions of the α- and γ-crystals of iPP mostly overlapped, and only the third ring of $(130)_\alpha$ and the fourth ring of $(117)_\gamma$ were different enough to identify α- and γ-crystals separately. The diffraction of $(130)_\alpha$, as the trace of α-crystals, was evident for every sample. Interestingly, the strong signal of $(117)_\gamma$ can be clearly identified in every layer of the OSIM samples in the rich M-iPP samples, while the signals were not clearly discernible in the CIM counterparts. The data reflect that the crystal structure and orientation are closely linked to the composition and processing method.

1D WAXD curves, which were extracted from 2D WAXD images, are presented in Fig. 3. As illustrated in Fig. 3a', the diffraction peaks are assigned to $(110)_\alpha$, $(040)_\alpha$, $(130)_\alpha$, $(111)_\alpha$, and $(041)_\alpha$ of the α-crystals [18] and to $(111)_\gamma$, $(008)_\gamma$, $(117)_\gamma$, $(202)_\gamma$, and $(026)_\gamma$ of the γ-crystals [19]. For clarity, the peaks of $(130)_\alpha$ and $(117)_\gamma$ are marked by dotted blue and red lines, respectively. In particular, the intensity of the $(117)_\gamma$ peak fluctuates for different blends, different processing methods, and different layers. For example, γ-crystals are almost missing in the curves of low M-iPP samples (e.g., MZ19 of CIM), while highly rich γ-crystals emerge in the intermediate layer of the high M-iPP samples (e.g., MZ91 of OSIM). On the other hand, only a few locations show a very weak signal for the β-phase, which may be caused by a mismatched shear rate and no β-nucleating agent [20]. Therefore, the effect of β-crystals is

Fig. 2 2D WAXD patterns at different depths from the surface of **a** CIM and **b** OSIM samples along the TD direction. The flow direction is vertical (samples of MZ19, MZ55, and MZ91 are presented as an illustration)
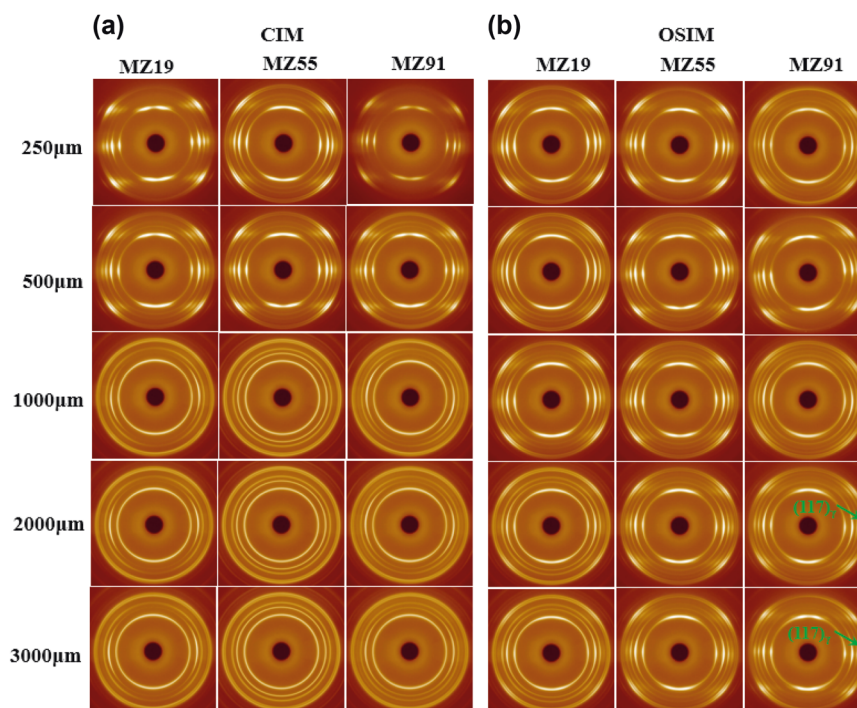
not considered in this study. Subsequently, the relative content of the γ-phase was calculated by Turner-Jones et al. as follows [21]:

$$f_\gamma = I_\gamma(117) / \left[I_\gamma(117) + I_\alpha(130) \right] \tag{3}$$

where $I(117)$ and $I(130)$ equate to the fitted diffraction areas of the peaks. Herein, f_γ can vary from 0 to 1 for samples containing γ-crystals from 0 to 100%.

The f_γ distribution through the depths of the blended samples is revealed in Fig. 4. For all CIM samples, f_γ is low in the skin layer and then gradually increases toward the core, showing the maximum value in the core layer of each blending composition. The lower cooling rate occurs in the core layer, which is reasonably supported by the increase in γ-form observed after the cooling rate is lowered and/or the crystallization temperature is increased [22–24]. More interestingly, f_γ at the inner locations increased with the M-iPP ratio, which explicitly occurred because M-iPP is more favorable to the formation of the γ-form than ZN-iPP [14, 25]. For the OSIM samples, f_γ initially increases and then decreases to a minimum at the inner position, the trend of which is different from that of the CIM samples. The prevailing view is that the γ-phase is thermodynamically preferred in the unoriented melt. However, in highly oriented OSIM samples, the nonmonotonic γ-phase content from the skin to the core is correlated with the epitaxial structure of highly oriented γ- and α-crystals, as reported in previous research [16]. This resultant structure can be attributed to the competition between flow-induced orientation and subsequent relaxation processes of chain

segments during the complex processing involved in OSIM technology. In addition, the maximum f_γ in the intermediate layer of the OSIM sample increased with increasing M-iPP content. It is distinct that the microstructure of the injected blending sample intensely depends on the external field (including shear and temperature) and blend composition.

As shown in Fig. 5, the 2D SAXS patterns at each depth of the CIM and OSIM samples allow us to discern the superstructure of crystals (orientation and spacing), thus providing persuasive evidence for the existence of shish-kebabs and/or spherulites [3, 26]. Normally, the streaks that are vertical to the flow direction stem from the scattering of shishes, while the maximal scattering parallel to the flow direction represents kebabs, signifying the formation of an oriented structure. In our cases, the two bulb-shaped lobes and equatorial streaks in the meridional direction in the SAXS pattern at 250 and 500 μm, both in CIM and OSIM samples, can be identified as a representative reflection of a shish-kebab. The maximal scattering parallel to the flow direction transforms from thin to broad for CIM samples toward the core, demonstrating a reduction in the lamellar orientation. For the OSIM samples, the shish-kebabs should be distributed throughout all the regions, while the undetected equatorial streaks with maximal scattering parallel to the flow direction in the core of the OSIM samples may be ascribed to the shish structures being slender or farther apart [27]. Generally, the intense shear flow in the OSIM substantially enhances the spatial occupation of shish-kebabs compared to the CIM samples.

Fig. 3 WAXD curves from the skin to the core of M-*i*PP/MZ-*i*PP blends by **a**–**c** CIM and **a'**–**c'** OSIM (samples of MZ19, MZ55, and MZ91 are presented as an illustration)
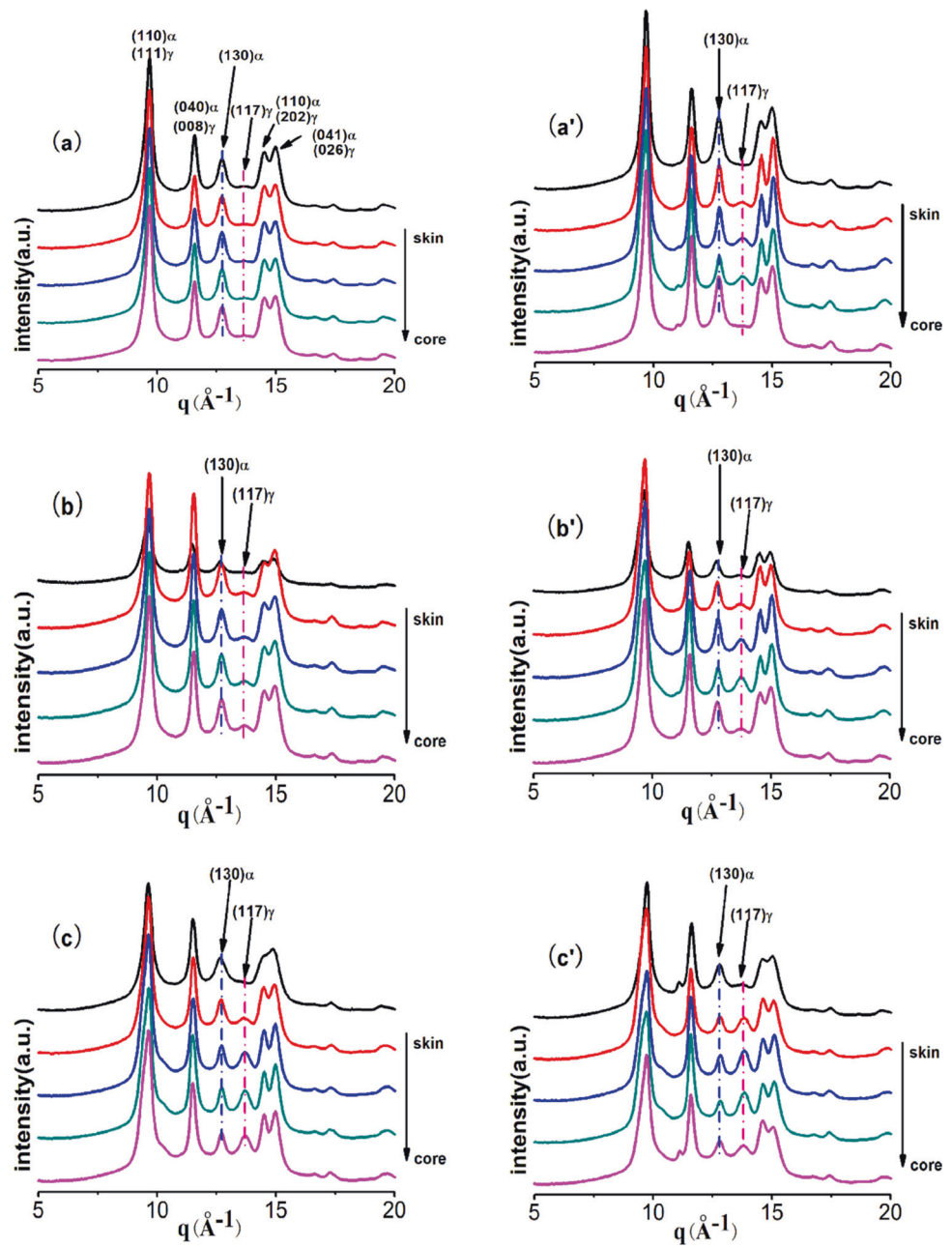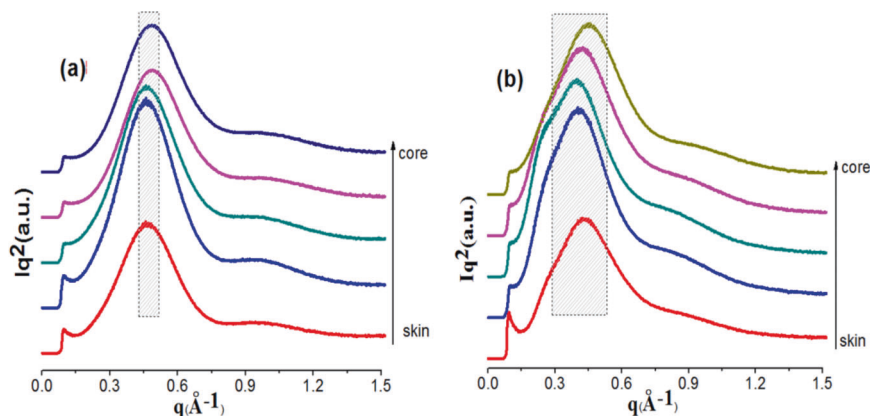

Fig. 4 Fraction of γ-crystal (*f*γ) calculated from the 1D WAXD profiles from each depth of the **a** CIM and **b** OSIM samples
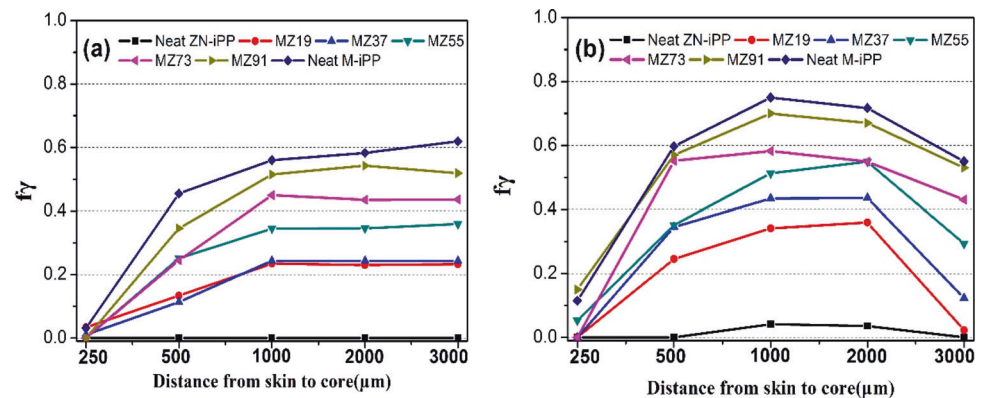
Fig. 5 2D SAXS patterns at each given depth of **a** CIM and **b** OSIM samples along the TD direction. The flow direction is vertical (samples of MZ19, MZ55, and MZ91 are presented as an illustration)
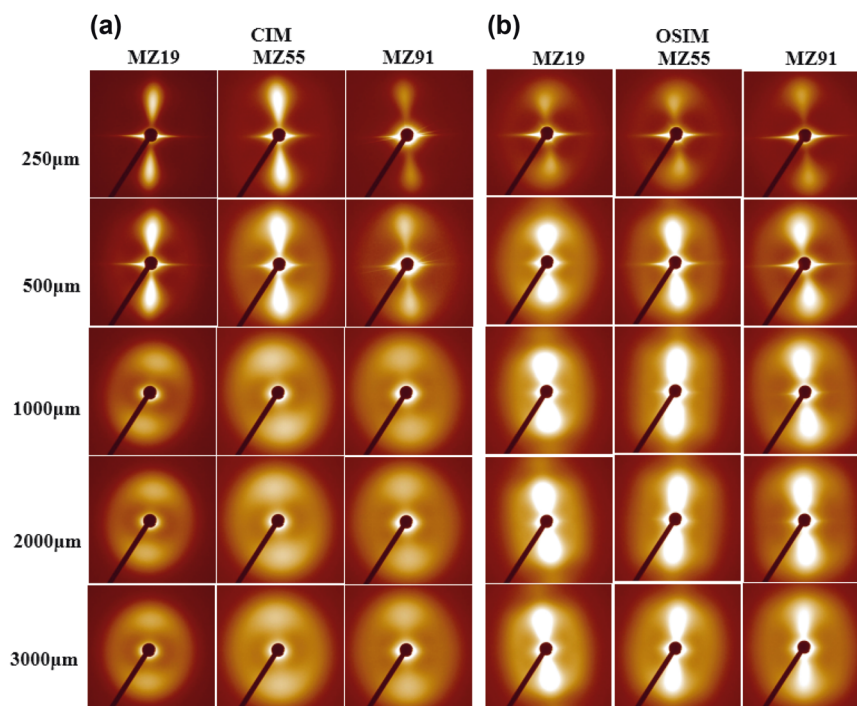
Fig. 6 Lorentz-corrected SAXS intensity profiles of **a** CIM and **b** OSIM

Lorentz-corrected intensity profiles of circularly integrated 2D SAXS patterns from the skin to the core, with the profiles of MZ55 as an example, are exposed in Fig. 6. A dominant scattering maximum of the typical profiles for *i*PP appears in all SAXS curves, while the range and spatial distribution of *q* between the CIM and OSIM samples are obviously different. According to Bragg's law, the long spacing ($L_B = 2\pi/q$), representing the width of the crystal and the amorphous region between two lamellae, is shown in Fig. 7. The L_B is generally consistent across all depths of each CIM sample, whereas the OSIM sample exhibits a maximum in the intermediate layer with a larger L_B than that of the CIM samples at almost every depth for each sample.

The overall crystallinity (X_c) of the blends was calculated after standard peak fitting of the WAXD profiles, as follows:

$$X_c = \frac{\sum A_{cryst}}{\sum A_{cryst} + \sum A_{amorp}}$$

Herein, the fitted areas of the crystalline and amorphous peaks were defined as A_{cryst} and A_{amorp}, respectively. The calculated crystallinity of the blends is displayed in Supplementary Table S1. The spatial crystallinity distribution shows little change for all kinds of blends in the CIM and OSIM samples. The lamellar thickness (d_c) was then generally calculated by multiplying L by X_c. The detailed d_c of the blends is shown in Supplementary Table S2. The OSIM samples exhibited a thicker d_c than that of the CIM samples, which could be attributed to the formation of thicker and more perfect lamellae due to the stronger shear flow, as well as the crystallization of melt at a higher temperature due to

Fig. 7 Long spacing (*L*) of the **a** CIM and **b** OSIM samples
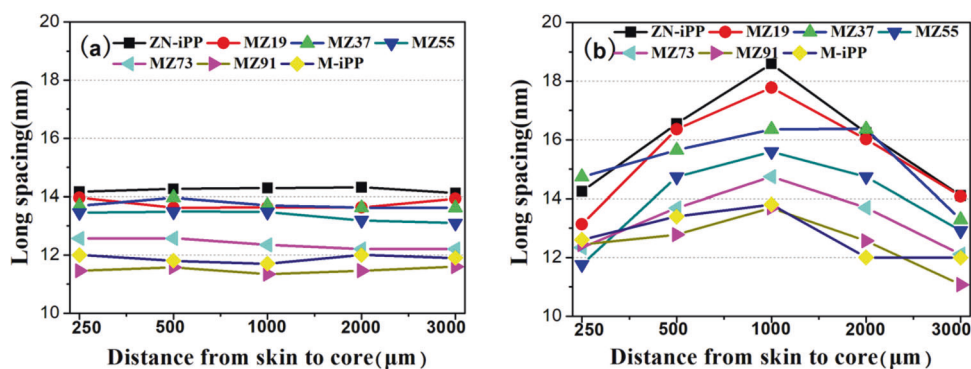
Fig. 8 Degree of molecular orientation (*f*$_H$) obtained from the calculation of the 040 and 008 reflections of **a** CIM and **b** OSIM samples by Hermans' orientation function
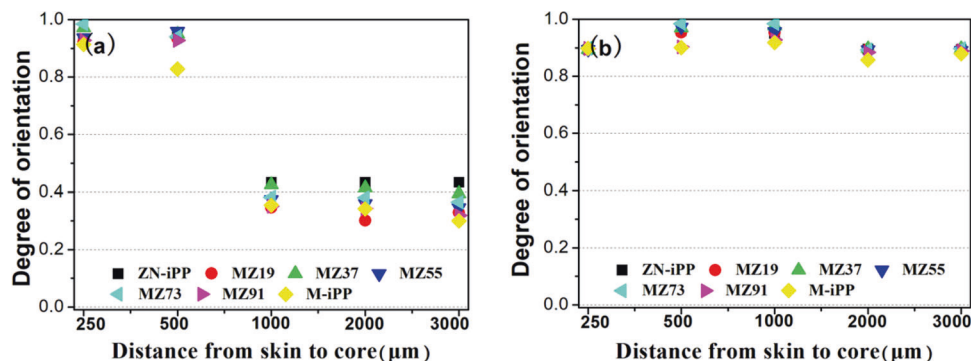
the lower cooling rate [28]. Furthermore, the d_c of both the CIM and OSIM samples decreased (Supplementary Table S2) with increasing M-*i*PP ratio at each position. Recalling the increase in M-*i*PP with the enhanced γ-crystal content, the decrease in d_c could be correlated with an enhancement in γ-crystal, which exhibits a relatively small size (Figs. 4 and 6) [22, 29]. Under this condition, the increase in M-*i*PP could enhance the γ-crystal content and consequently decrease the thickness of the lamellae, which might reduce the yield stress of the injection-molded specimen [30, 31].

Molecular orientation

The global orientation of two types of crystals (α- and γ-phases) was exploited based on the azimuthal profiles at $q = 9.70\,\text{Å}^{-1}$, and the calculated f_H is shown in Fig. 8. For CIM, the value of f_H at the 250 μm depth reaches 0.94 and then maintains a high degree of orientation at 500 μm but suddenly decreases to 0.30–0.43 toward the core (3000 μm). For the OSIM sample, f_H only slightly decreases from the skin to the core and is maintained at a very high level (0.86–0.96) due to continuous shear during cooling.

The azimuthal profiles at $q = 9.70\,\text{Å}^{-1}$ represent the superposition of two kinds of crystal (α- and γ-crystal) orientations and the cancellation of the diffraction from the parents and daughters of the α-crystal to the axis orientation. To exploit the orientation of the α- and γ-phases, the azimuthal distributions of $(130)_\alpha$ at $q = 12.76\,\text{Å}^{-1}$ and

$(117)_\gamma$ at $q = 13.81\,\text{Å}^{-1}$ were studied, as shown in Fig. 9, which correspond to the orientations of the α- and γ-phases, respectively. The azimuthal $(130)_\alpha$ diffraction exhibits a three-peak type (Fig. 9a, b), meaning that the α-oriented crystals display a typical parent−daughter lamellae structure. Such a parent−daughter structure suggests that the growing daughter lamellae tilted approximately 81° on parent lamellae [32]. For the γ-crystals, the azimuthal profiles of $(117)_\gamma$ exhibit three peaks (Fig. 9c, d) for all OSIM samples and the skin of the CIM sample. The orthorhombic γ-phase is composed of adjacent bilayers tilted by 80 or 100° from one another [33]. The three peaks in the azimuthal profiles of the γ-crystal indicate that one-half of the chain axes are parallel to the reference axis, and the other half is tilted approximately 81° with respect to the reference axis. This kind of orientation is denoted as "parallel chain axis orientation" [29], which occupies the highly oriented area of injection-molded parts. Complex oriented specimens, as well as varied f_γ, exert a profound effect on mechanical performance.

Thermal analysis

The DSC curves for injection-molded specimens with various ZN-*i*PP/M-*i*PP ratios are presented in Fig. 10. The DSC curves of the samples show two main endothermic peaks. Combined with the WAXD results, the T_m of the higher and lower temperatures matches the melted α-crystals and γ-crystals, respectively. With an increased amount

Fig. 9 Azimuthal profiles I(φ) of the $(130)_\alpha$ and $(117)_\gamma$ reflections with azimuthal angle φ through the depth of the MZ55 sample: **a** $(130)_\alpha$ of the CIM sample, **b** $(130)_\alpha$ of the OSIM sample, **c** $(117)_\gamma$ of the CIM sample, and **d** $(117)_\gamma$ of the OSIM sample
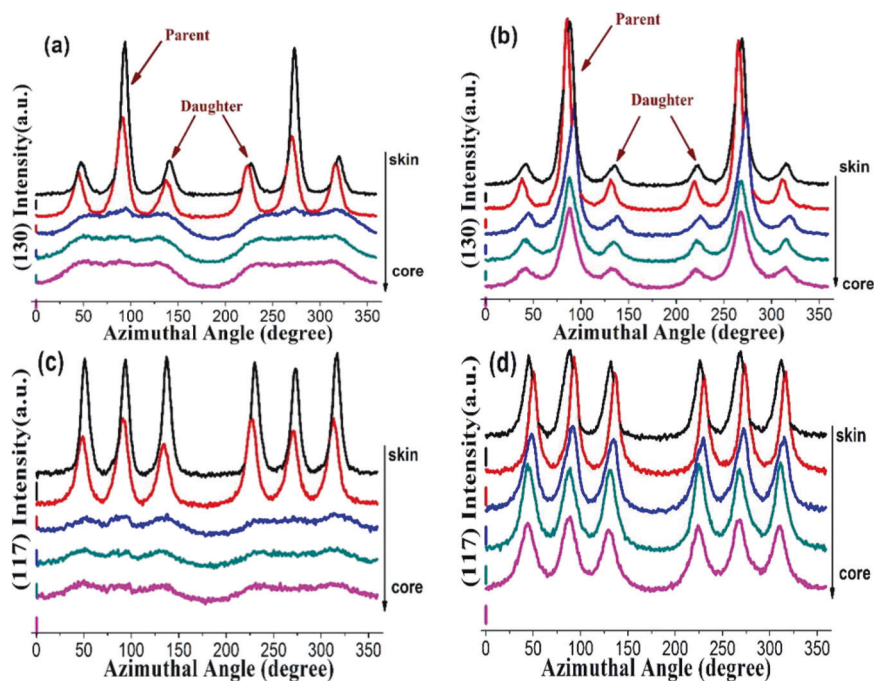
Fig. 10 DSC melting thermographs of **a** MZ19, **b** MZ55, and **c** MZ91. **d** Melting temperature (T_m) of α-crystals with different ZN-iPP contents
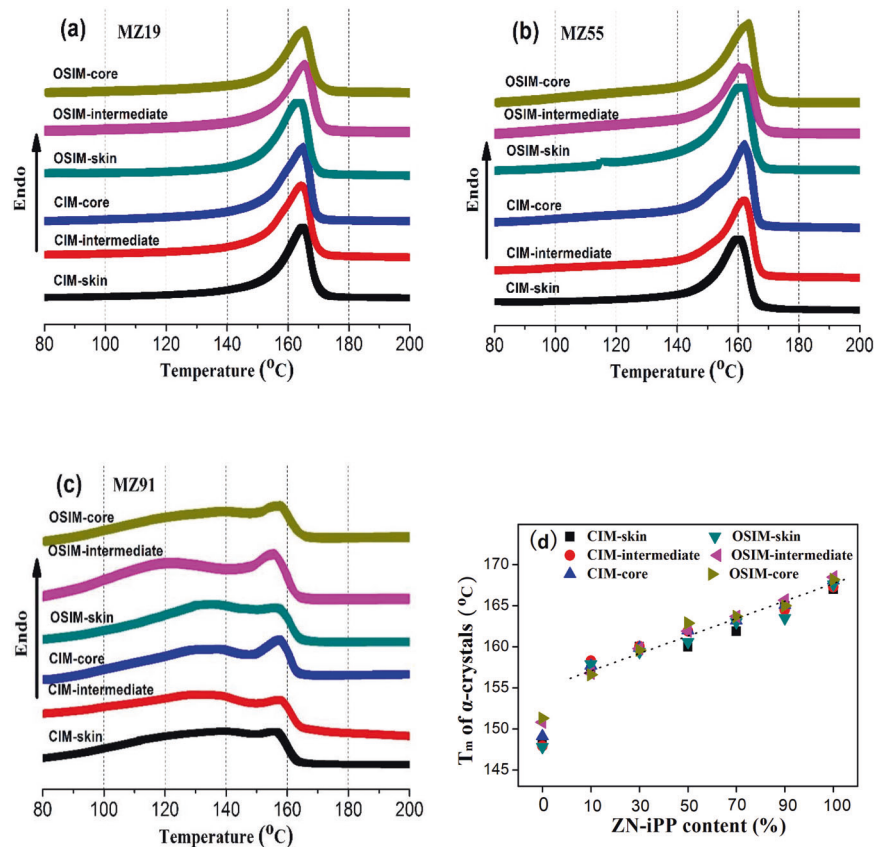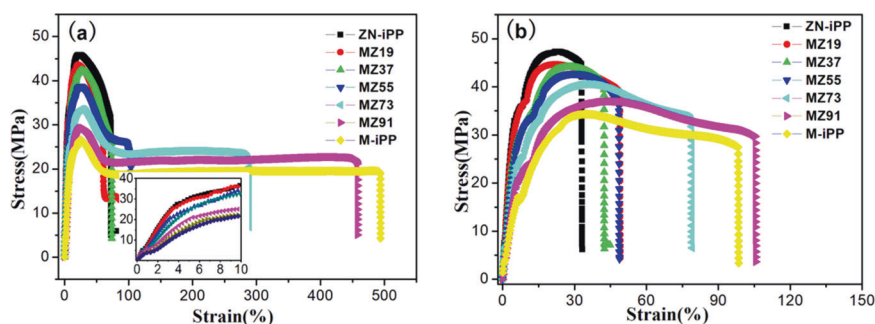
of M-iPP, the γ-crystals became more obvious. Furthermore, it is interesting to observe that the T_m of α-crystals increased with increasing ZN-iPP content. A linear variation in the T_m of α-crystals with the ZN-iPP content is

evidenced, as illustrated in Fig. 10d, indicating that the thickness of α-iPP lamellae is incrementally enhanced due to the increase in ZN-iPP. However, the sharp decrease in the T_m of α-crystals for pure M-iPP may have occurred

because the nucleation of α-crystals for pure M-*i*PP was somewhat different from the blends that were intervened by ZN-*i*PP. Incidentally, further observation shows that the varied peak area is roughly observed in different layers of the injection sample of each component, representing the change in the number of α- and γ-crystals, which is in concordance with the WAXD results (Figs. 2–4).

Mechanical properties

Figure 11 represents the stress–strain curves of the M-*i*PP and ZN-*i*PP blends. The main feature of both the CIM and OSIM samples is a ductile fracture with obvious yield and necking. The elastic area of tensile testing is magnified in Fig. 11a, and the stiffness was enhanced with increasing ZN-*i*PP. The summarized mechanical properties indicate that the tensile strength of the CIM samples gradually varied from 26.9 to 46.0 MPa with the enhancement of ZN-*i*PP (Fig. 12a), and the same tendency applied to Young's modulus (Fig. 11b). In contrast, a drastic decline in impact strength was observed with increasing ZN-*i*PP loading (Fig. 12c). The impact strength of pure ZN-*i*PP is only 4.7 kJ/m^2, reflecting the notoriously low toughness, which is a problem of commercial polypropylene. Herein, the toughness (maximum value 13.5 kJ/m^2) was improved with the weakened tensile strength and modulus to some extent with the increasing M-*i*PP ratio. Therefore, by varying the blend composition, the mechanical properties can be changed from stiff to ductile. Compared to the counterpart CIM sample, the OSIM samples exhibited a greater promotion in the tensile strength (Fig. 12a), Young's modulus (Fig. 12b), and impact strength (Fig. 12c). Taking pure M-*i*PP as an example, the tensile strength, Young's modulus, and impact strength increased by 30%, 70% and 73%, respectively, from 26.9 MPa, 143 MPa and 13.5 kJ/m^2 for the CIM samples to 34.5 MPa, 243 MPa, and 23.3 KJ/m^2 for the OSIM samples, respectively. Moreover, the impact strength of the OSIM samples significantly outperforms that of their CIM counterparts, in addition to the outstanding strength and modulus. Furthermore, when the ZN-*i*PP content is greater than or equal to 30 wt %, the tensile strength is higher than 40.8 MPa, and the impact strength

remains at the high level of 14.2–18.9 KJ/m^2, realizing simultaneous enhancement in both strength and toughness at different polypropylene blending ratios.
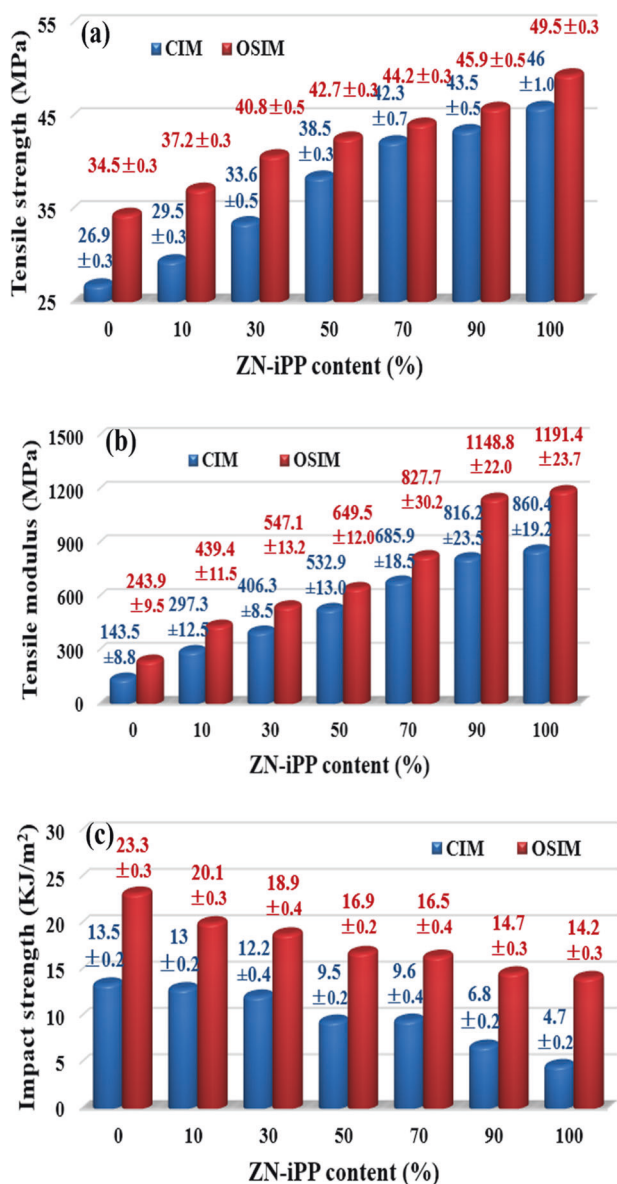
Discussion

Through microscopic insight into the crystallization and mechanical properties of *i*PP blends, the following interesting findings were obtained: (1) In contrast to the use of different catalysts for the desired property, the blends depending on the composition could gradually vary from highly stiff to ductile thermoplastic materials; (2) compared to CIM, the OSIM samples exhibited greater reinforcement and toughening at a given blend composition.

Tunable mechanical properties upon simple blending

Blending with thermoplastic elastomer or rubber [34] and compounding with organic or inorganic fillers [35, 36] has been widely applied to achieve the balanced mechanical performance of *i*PP. However, these methods often face challenges, such as dispersion, phase interface formation, and compatibility. In this research, two kinds of chemically similar *i*PP were mixed to eliminate the aforementioned drawbacks due to the benign miscibility of these *i*PPs in the melt [7, 37, 38]. In addition, because of the chemical similarity of M-*i*PP and ZN-*i*PP, their weak mutual interactions facilitate the rearrangement of the M-*i*PP/ZN-*i*PP blend chains [6, 39]. The single exothermic peak, as shown in Supplementary Fig. S1, indicates that the macrocrystalline phase of the blends is uniform and likely forms mixed lamellar stacks in blending systems [6, 7, 38].
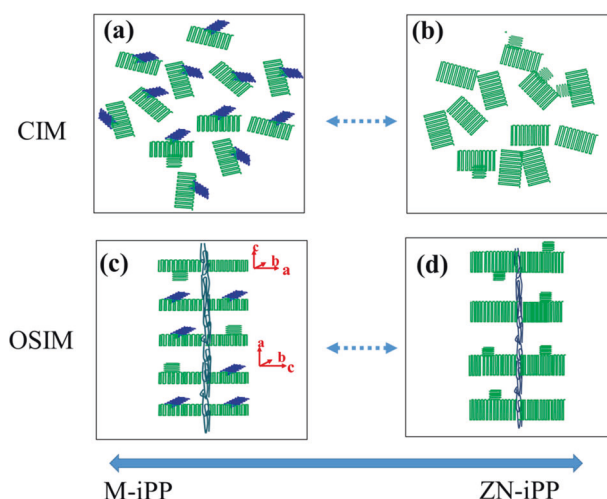
Notably, γ-crystal content tends to increase with increasing M-*i*PP (Figs. 4a and 10d) because the small size of the γ-crystal could grow on any available α-crystals [32, 40, 41]. Furthermore, the mixed lamellar stacks imply that the branching of the readily available γ-crystals in M-*i*PP not only grows on the α-lamellae originating from M-*i*PP but can also grow directly on those from ZN-*i*PP. This is supported by the knowledge that the T_m of α-crystals

Fig. 12 **a** Tensile strength, **b** tensile modulus, and **c** impact strength with different ZN-*i*PP contents

Fig. 13 Morphological schematic of the CIM and OSIM samples. The transition from (**a**) to (**b**) represents a shift from M-iPP being the major component to an overabundance of ZN-iPP, and the transition from (**c**) to (**d**) is the same (green lamellar: parent lamellae and daughter lamellae of α-crystals, blue lamellar: γ-lamellae)

and hierarchical structures of injection molding, which are achieved by changing the M-*i*PP/ZN-*i*PP ratio, naturally generate varied mechanical properties. The results in Fig. 12a, b and Supplementary Table S2 indicate that the increase in tensile strength for the molded specimen was accompanied by an increase in lamellae thickness, which is supported by a previous report in which thicker lamellae showed higher resistance to interlamellar slip [30, 31]. On the other hand, the enhanced lamellar thickness results in a reduction in the impact strength (Fig. 12c) and the elongation at break (Fig. 11a). It is inconceivable that the advantage of binary *i*PP blends that exhibit different properties from the CIM samples is achieved simply by simply blending two different kinds of *i*PP.

Improved comprehensive properties for the OSIM samples

For OSIM processing, blends endure strong flow and non-isothermal crystallization processing. As shown in the model diagrams of Fig. 13c, d, the key character across the OSIM samples is the well-known lamella-branched shish-kebab structure, consisting of the shish-structure of the extended chain, kebabs (parents), and daughter lamellae of the folded chain [42]. In addition, combined with the azimuthal scan in Fig. 9, all orientations of the α-phase with c-axes and γ-phase with a-axes aligned flow direction are shown schematically in Fig. 13c, indicating that the γ-crystals are oriented on α-crystals driven by epitaxy lattice matching [41]. In fact, shish-kebabs of *i*PP with oriented crystals can result in remarkable reinforcement [10, 43, 44]. In this work, compared to the CIM samples, M-*i*PP/ZN-*i*PP

within all blends is much lower than the T_m of α-crystals of the ZN-*i*PP homopolymer, as shown in Fig. 10d. In summary, the increased M-*i*PP enhances the γ-crystal content (Fig. 4a) and thus facilitates the formation of thinner lamellae in the mixed lamellar stacks (Supplementary Table S2), which are schematically proposed in Fig. 13b to a and likewise in Fig. 13d to c.

As illustrated in Supplementary Table S1, the total crystallinity of the M-*i*PP/ZN-*i*PP blends remains basically unchanged with the blend component, demonstrating that the crystallization capacity is not greatly influenced by the various components. Therefore, the crystallinity of the blends hardly contributes to the altered mechanical performance. It is natural to conclude that the varied polymorphic

exhibited synchronous reinforcement and toughening for all components, as shown in Fig. 12a, c. Furthermore, more γ-crystals are formed in rich M-*i*PP blends, resulting in a thinner lamellar thickness and thereby leading to a certain decrease in tensile strength, as diagrammed in Fig. 13d to c.

It is worth stressing that the tensile strength is unsatisfactory in the rich M-*i*PP blending and CIM samples as a result of the thin lamellar thickness and nonpenetrating orientation. In the present work, such a drawback could be compensated by the oriented crystals. In contrast, an unsatisfactory impact toughness (Fig. 12c) for the rich ZN-*i*PP samples was also dramatically elevated by increasing M-*i*PP and/or applying the OSIM technology. As is widely discussed in this paper, varied properties ranging from high stiffness, typical of neat ZN-*i*PP, to ductile material, typical of neat M-*i*PP, are realized by simply blending *i*PP samples. Furthermore, while the components of blends are not changed, the regulation of the hierarchical structure of blends based on orientation induced by shear stress can also effectively promote strength and stiffness. Considering the large commercial importance, we firmly believe that our strategy could help elaborate the complicated morphology, which can tailor the properties and extend the application scope of *i*PP.

Conclusions

We conducted a comprehensive study of the structure and mechanical properties of M-*i*PP/ZN-*i*PP blends based on their compositions and processing conditions. A continuous change in tensile strength (26.9–49.5 MPa) and impact strength (4.7–23.2 KJ/m^2) of *i*PP samples was successfully accomplished without using specific catalysts. On the one hand, more γ-crystals and thinner lamellae thickness in the blend with higher M-*i*PP cause the diminishment of tensile strength; however, this drawback could be compensated by the increased ZN-*i*PP components. In contrast, the impact toughness for the ZN-*i*PP samples was dramatically elevated by increasing M-*i*PP. On the other hand, after applying the OSIM technology, the hierarchically oriented shish-kebab morphology observed in the samples significantly and simultaneously reinforced and toughened the injection-molded *i*PP blends. Our results provide a facile and effective method for tailoring the mechanical behavior of *i*PP blends by controlling the crystallinity and orientation of the hierarchical morphology depending on the composition and processing conditions.

Compliance with ethical standards

Conflict of interest The authors declare no competing interests.

References

1. Jasinska-Walc L, Bouyahyi M, Duchateau R. Potential of functionalized polyolefins in a sustainable polymer economy: synthetic strategies and applications. Acc Chem Res. 2022;55:1985–96.
2. Garcia JM, Robertson ML. The future of plastics recycling. Science. 2017;358:870–2.
3. Zhang Z, Lei J, Chen Y, Chen J, Ji X, Tang J, et al. Tailored structure and properties of injection-molded atactic polypropylene/isotactic polypropylene blend. ACS Sustain Chem Eng. 2013;1:937–49.
4. Zhou M, Mi D, Hou F, Zhang J. Tailored crystalline structure and mechanical properties of isotactic polypropylene/high molecular weight polyethylene blend. Ind Eng Chem Res. 2017;56:8385–92.
5. Graziano A, Jaffer S, Sain M. Review on modification strategies of polyethylene/polypropylene immiscible thermoplastic polymer blends for enhancing their mechanical behavior. J Elastomers Plast. 2019;51:291–336.
6. Auriemma F, Ballesteros ORD, Rosa CD, Invigorito C. Tailoring the mechanical properties of isotactic polypropylene by blending samples with different stereoregularity. Macromolecules. 2011;44:6026–38.
7. Auriemma F, Ruiz de Ballesteros O, De Rosa C. Theoretical investigation of nano-scale organization in blends of semi-crystalline/semicrystalline polymers by small angle X-ray scattering. Macromolecules. 2010;43:9787–801.
8. Seyedi M, Savchak M, Tiiara A, Luzinov I. Toward mechanical recycling of polystyrene/polypropylene blends with bottlebrush-modified graphene oxide as a compatibilizer. ACS Appl Mater Interfaces. 2022;14:35074–86.
9. Su Y, Huang P, Zhao Y, Zheng W, Lan X, Luo H, et al. Lightweight polypropylene/polylactic acid composite foams with controllable hollow radially gradient porous structures for oil/water separation. Ind Eng Chem Res. 2022;61:10982–9.
10. Schrauwen BAG, Breemen LCAV, Spoelstra AB, Govaert LE, Peters GWM, Meijer HEH. Structure, deformation, and failure of flow-oriented semicrystalline polymers. Macromolecules. 2004;37:8618–33.
11. Wang K, Chen F, Li Z, Fu Q. Control of the hierarchical structure of polymer articles via "structuring" processing. Prog Polym Sci. 2014;39:891–920.
12. Chen YH, Zhong GJ, Wang Y, Li ZM, Li L. Unusual tuning of mechanical properties of isotactic polypropylene using counteraction of shear flow and β-nucleating agent on β-form nucleation. Macromolecules. 2009;42:4343–8.
13. Lezak E, Bartczak Z, Galeski A. Plastic deformation of the γ phase in isotactic polypropylene in plane-strain compression. Macromolecules. 2006;40:4933–41.
14. Rosa CD, Auriemma F, Spera C, Talarico G, Tarallo O. Comparison between polymorphic behaviors of ZieglerNatta and Metallocene-made isotactic polypropylene: the role of the distribution of defects in the polymer chains. Macromolecules. 2004;37:1441–54.
15. Caelers HJM, Govaert LE, Peters GWM. The prediction of mechanical performance of isotactic polypropylene on the basis of processing conditions. Polymer. 2016;83:116–28.
16. Wang Y, Pan J-L, Mao Y, Li Z-M, Li L, Hsiao BS. Spatial distribution of γ-crystals in metallocene-made isotactic polypropylene crystallized under combined thermal and flow fields. J Phys Chem B. 2010;114:6806–16.

17. Picken SJ, Aerts J, Visser R, Northolt MG. Structure and rheology of aramid solutions: x-ray scattering measurements. Macromolecules. 1990;23:3849–54.
18. Natta G, Corradini P. Structure and properties of isotactic polypropylene. Nuovo Cimento Suppl. 1960;15:40–51.
19. Brückner S, Meille SV. Non-parallel chains in crystalline -isotactic polypropylene. Nature. 1989;340:455–7.
20. Yang SG, Chen YH, Deng BW, Lei J, Li L, Li ZM. Window of pressure and flow to produce β-crystals in isotactic polypropylene mixed with β-nucleating agent. Macromolecules. 2017;50:4807–16. acs.macromol.7b00041.
21. Jones AT, Aizlewood JM, Beckett DR. Crystalline forms of isotactic polypropylene. Macromol Chem Phys. 1964;75:134–58.
22. Auriemma F, De Rosa C. Crystallization of metallocene-made isotactic polypropylene: disordered modifications intermediate between the α and γ forms. Macromolecules. 2002;35:9057–68.
23. Foresta T, Piccarolo S, Goldbeck-Wood G. Competition between α and γ phases in isotactic polypropylene: effects of ethylene content and nucleating agents at different cooling rates. Polymer. 2001;42:1167–76.
24. Xie XL, Yue L, Xu JZ, Zheng Y, Zhong GJ, Li ZM. Largely enhanced mechanical performance of poly(butylene succinate) multiple system via shear stress-induced orientation of the hierarchical structure. J Mater Chem A. 2018;55:1985–96. 10.1039.C8TA03778G-.
25. Alamo RG, Kim MH, Galante MJ, Isasi JR, Mandelkern L. Structural and kinetic factors governing the formation of the γ polymorph of isotactic polypropylene. Macromolecules. 1999;32:4050–64.
26. Xie X-L, Li Y, Xu J-Z, Yan Z, Zhong G-J, Li Z-M. Largely enhanced mechanical performance of poly (butylene succinate) multiple system via shear stress-induced orientation of the hierarchical structure. J Mater Chem A. 2018;6:13373–85.
27. Kumaraswamy G, Verma RK, Kornfield JA, Yeh F, Hsiao BS. Shear-enhanced crystallization in isotactic polypropylene. In-situ synchrotron SAXS and WAXD. Macromolecules. 2004;37:9005–17.
28. Xie X-L, Li Y, Xu J-Z. Largely enhanced mechanical performance of poly(butylene succinate) multiple system via shear stress-induced orientation of the hierarchical structure. J Mater Chem A. 2018;6:13373–85.
29. Auriemma F, De Rosa C. Stretching isotactic polypropylene:? From "cross-β" to crosshatches, from γ form to α form. Macromolecules. 2006;39:7635–47.
30. Kazmierczak T, Galeski A, Argon AS. Plastic deformation of polyethylene crystals as a function of crystal thickness and compression rate. Polymer. 2005;46:8926–36.
31. Chang B, Schneider K, Xiang F, Vogel R, Roth S, Heinrich G. Critical strains for lamellae deformation and cavitation during uniaxial stretching of annealed isotactic polypropylene. Macromolecules. 2018;51:6276–90.
32. Lotz B, Wittmann JC. The molecular origin of lamellar branching in the α (monoclinic) form of isotactic polypropylene. J Polym Sci B Polym Phys. 1986;24:1541–1558.
33. Meille SV, Brückner S. Non-parallel chains in crystalline γ-isotactic polypropylene. Nature. 1989;340:455–7.
34. Bucknall CB, Soares V, Yang H, & Zhang X. Rubber toughening of plastics: Rubber particle cavitation and its consequences[J]. Macromolecular Symposia. 1996;265–71.
35. Karnani R, Krishnan M, Narayan R. Biofiber-reinforced polypropylene composites. Polym Eng Sci. 1997;37:476–83.
36. Thio Y, Argon A, Cohen R, Weinberg M. Toughening of isotactic polypropylene with CaCO3 particles. Polymer. 2002;43:3661–74.
37. Reddy KR, Tashiro K, Sakurai T, Yamaguchi N. Cocrystallization phenomenon between the H and D species of isotactic polypropylene blends as revealed by thermal and infrared spectroscopic analyses for a series of D/H blend samples. Macromolecules. 2008;41:9807–13.
38. Reddy KR, Tashiro K, Sakurai T, Yamaguchi N. Isotope effect on the isothermal crystallization behavior of isotactic polypropylene blends between the deuterated and hydrogenated species. Macromolecules. 2009;42:1672–8.
39. Mandelkern L. Crystallization of polymers. Volume 1. Equilibrium concepts. Cambridge University Press: Cambridge, UK and New York; 2002.
40. Lotz B, Graff S, Straupe C, Wittmann J. Single crystals of γ phase isotactic polypropylene: combined diffraction and morphological support for a structure with non-parallel chains. Polymer. 1991;32:2902–10.
41. van Erp TB, Balzano L, Peters GWM. Oriented gamma phase in isotactic polypropylene homopolymer. ACS Macro Lett. 2012;1:618–22.
42. Yang S-G, Zhang Z, Zhou D, Wang Y, Lei J, Li L, et al. Flow and pressure jointly induced ultrahigh melting temperature spherulites with oriented thick lamellae in isotactic polypropylene. Macromolecules. 2015;48:5834–44.
43. Kalay G, Bevis MJ. Processing and physical property relationships in injection-molded isotactic polypropylene. 1. Mechanical properties. J Polym Sci B Polym Phys. 1997;35:241–63.
44. Mi D, Xia C, Jin M, Wang F, Shen K, Zhang J. Quantification of the effect of shish-kebab structure on the mechanical properties of polypropylene samples by controlling shear layer thickness. Macromolecules. 2016;49:4571–8.